Journal of Power Sources 451 (2020) 227799

Contents lists available at ScienceDirect

Journal of Power Sources

journal homepage: www.elsevier.com/locate/jpowsour

Metal-free N-doped ultrafine carbon fibers from electrospun Polymers of Intrinsic Microporosity (PIM-1) based fibers for oxygen reduction reaction

Bhushan Patil [a,*], Bekir Satilmis [a,b,**], Tamer Uyar [a,c,***]

[a] Institute of Materials Science and Nanotechnology, Bilkent University, Ankara, 06800, Turkey
[b] Department of Medical Services and Techniques, Vocational School of Health Services, Kirsehir Ahi Evran University, Kirsehir, 40100, Turkey
[c] Department of Fiber Science & Apparel Design, College of Human Ecology, Cornell University, Ithaca, NY, 14853, USA

HIGHLIGHTS

- Electrospinning of amide, amine and amidoxime based PIM-1 fibers.
- Synthesis and characterization of N-doped carbon fibers from electrospun fibers.
- Influence of functional groups in the fibers towards oxygen reduction reaction.
- Position of nitrogen and conductivity of fibers are crucial towards ORR catalysis.

GRAPHICAL ABSTRACT

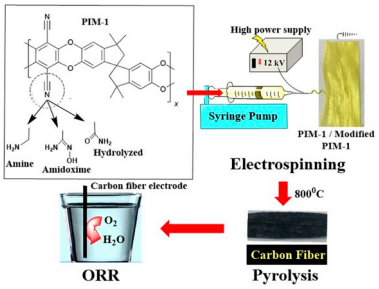

ARTICLE INFO

Keywords:
Polymers of intrinsic microporosity
Catalyst
Electrospinning
Carbon nanofibers
Oxygen reduction reaction

ABSTRACT

Synthesis of nitrogen-doped carbon fibers (CF) has been proved to be one of the most promising oxygen reduction reaction (ORR) catalysts which can replace the state-of-art Pt catalyst for non-noble metal-free light-weight devices. Polymers of Intrinsic Microporosity (PIM-1) is soluble in common organic solvents and can be tailored by functionalization owing to nitrile groups in the backbone. PIM-1 was functionalized to amide (hydrolyzed PIM-1), amine and amidoxime groups. The modified PIM-1s were electrospun into ultrafine fibers and pyrolyzed to obtain CF. The present article investigates the influence of different functional groups on the properties of PIM-1 based CF and their nitrogen-doping. Particularly, their ORR performance has been evaluated. Interestingly, CF from hydrolyzed PIM-1 have the highest pore volume with small pore size among the CF based on PIM-1, amine and amidoxime PIM-1. The amount of nitrogen-doping in these CF shows the trend according to the functional groups as PIM-1 > amine > amidoxime > amide. Among all these PIM-1 based CF; CF from hydrolyzed PIM-1 has the highest percentage of pyridinic and graphitic nitrogen, furthermore, electrocatalysis revealed that ORR processed through four-electron with the onset potential 985 mV vs. reversible hydrogen electrode (RHE) which is comparable with the standard Pt/C catalysts.

* Corresponding author.
** Corresponding author. Institute of Materials Science and Nanotechnology, Bilkent University, Ankara, 06800, Turkey
*** Corresponding author. Institute of Materials Science and Nanotechnology, Bilkent University, Ankara, 06800, Turkey
E-mail addresses: bhushanpatil25@gmail.com (B. Patil), bekir.satilmis@ahievran.edu.tr (B. Satilmis), tu46@cornell.edu (T. Uyar).

https://doi.org/10.1016/j.jpowsour.2020.227799
Received 3 September 2019; Received in revised form 29 November 2019; Accepted 23 January 2020
Available online 7 February 2020

1. Introduction

Carbon is abundant and widely used electrode material in the electrochemical applications due to its easy tunable properties by altering allotropes [1], morphology [2], sp^2-sp^3 hybridization [3], dimensions [4,5], conductivity control [6], easy to dope with numerous elements [7], quantum confinement [8], etc. Electrospinning is a convenient technique to produce nanofibers and ultrafine fibers from variety of materials for various applications in the field of healthcare, environment, sensors, and energy [9,10]. Numerous electrospun ultrafine fibers have been produced from a variety of different materials such as polyacrylonitrile (PAN) [11], polyvinylidene fluoride (PVDF) [12], lignin [13], and Polymers of Intrinsic Microporosity (PIM-1) [14,15], and these electrospun ultrafine fibers were used as precursors for the preparation of carbon nanofibers/microfibers. Among all these polymers, PIM-1 based electrospun fibers have the high surface area and proved to be readily functionalized with different functional groups [16–18]. Recently, we have reported the use of PIM-1 based electrospun nitrogen-doped carbon fibers (CF) for the free-standing, flexible and stable electrode material [15]. Modification or functionalization of PIM-1 based fibers with different functional groups alters the morphology of nitrogen and the total amount of nitrogen content in the CF. Thus, amide, amine, and amidoxime functionalized PIM-1 based electrospun fibers were selected for this study. These PIM-1 based electrospun fibers were pyrolyzed at identical conditions to obtain CF and used as electrocatalyst for oxygen reduction reaction (ORR) in alkaline medium. To the best of our knowledge, this is the first report which presents CF pyrolyzed from amide, amine, and amidoxime functionalized PIM-1 based electrospun fibers and their catalytic activity towards ORR.

The ORR is the sluggish and rate limiting step in the fuel cells and metal air batteries. It leads to finding out catalysts to enhance the ORR kinetics with 4-electron reaction without H_2O_2 production [19–21]. Although, Pt is considered as the best ORR catalyst, its high-cost and surface-poisoning limits the potential use of Pt as ORR catalysts [22,23]. Alternatively, non-noble catalysts were analyzed and can be proved to be efficient electrocatalysts towards ORR such as Ni, Co, Fe, etc. [24,25]. Lowering the amount of catalyst or increasing the mass activity of catalyst is highly desirable for the commercialization of the polymer electrolyte membrane fuel cell (PEMFC), perovskites and metal air batteries [21,24,26]. The mass activity of catalyst directly influences ORR in the PEMFC [27] and metal air batteries [28,29]. To achieve the highest catalytic activity of ORR with less amount of metal catalyst, it is necessary to obtain high mass activity. Furthermore, metal-free ORR catalyst is one of the great interests in the scientific community to achieve light-weight equipment like metal-air batteries, fuel cells, etc. Heteroatom-doped carbon is one of the widely studied material for metal-free devices [30,31]. Nitrogen-doped carbon (N-doped carbon) has proved to be an effective catalyst towards ORR, showing 4-electron oxygen reduction [30,32–34]. In addition, the position of the nitrogen doping plays a crucial role in ORR catalysis which demands specific N-doped carbon for such application [35]. The studies have been reported which shows poor catalytic activity of N-doped carbon in the acidic medium whereas, N-doped carbon is more active in the alkaline medium due to oxophilic nature of N-doped carbon [36–38].

PIM-1 based fibers with amide, amine, and amidoxime functional groups have been reported and showed different properties [39–41], thus, we have selected these modified PIM-1s and electrospun into ultrafine fibers as a precursor for the CF preparation. An influence of these functional groups on the properties of carbon fibers such as surface area, morphology, amount of nitrogen doping and position of nitrogen in the carbon fibers have been disclosed. The ORR is mainly influenced by the morphology, the amount of nitrogen and position of nitrogen doping in the carbon lattice. Thus, preparation of controlled morphology with nitrogen doping is the challenge for N-doped carbon catalyst. To achieve this, we have attempted to integrate electrospinning and pyrolysis for the synthesis of CF from the PIM-1 based fibers to reveal an influence of functional groups of PIM-1 in the amount of nitrogen content and its position towards ORR under alkaline medium.

2. Experimental

2.1. Materials

The chemicals 5,5′,6,6′-Tetrahydroxy-3,3,3′,3′-tetramethyl-1,1′-spirobisindane (TTSBI, 98%), tetrafluoroterephthalonitrile (TFTN, 98%), K_2CO_3 (99%) were obtained from Alfa Aeser and were purified according to the reported procedure [42]. Borane-dimethylsulfide complex (5.0 M in diethyl ether), hydroxylamine (50% in H_2O), dimethylacetamide (DMAc, ≥99.9%), toluene (99.9%), 1,1,2,2 tetrachloroethane (98%), ethanol (EtOH, ≥99.8%), chloroform ($CHCl_3$, 99–99.4%), tetrahydrofuran (THF, ≥99.9%), methanol (MeOH, ≥99.8%), dimethyl sulfoxide (DMSO, ≥99.9%), sodium hydroxide (NaOH, pellets), dimethylformamide (DMF, ≥99.8%), hydrochloric acid (HCl, 37%), potassium hydroxide (KOH, pellets), and Pt/C (20% Pt, <5 nm size) were purchased from Sigma Aldrich. Nafion (5%) was obtained from Dupont. All the chemicals were used without further treatment unless specified. 18 MΩ Milli-Q water was used for the preparation of aqueous solutions.

2.2. Synthesis and electrospinning of PIM-1 based fibers

2.2.1. Synthesis and electrospinning of PIM-1

Synthesis of PIM-1 powder was achieved as reported previously [16]. Briefly, TTSBI and TFTN were reacted in the presence of K_2CO_3 catalyst in DMAc-toluene solvent mixture at 160 °C for 40 min. The crude polymer was first dissolved in chloroform and then precipitated in methanol, and subsequently reflux in deionized water for 4h. The polymer was dried at 110 °C for 48h. Yield: 62 g (90%). Gel permeation chromatography (GPC): $M_n = 106{,}000$, $M_w = 189{,}000$, $M_w/M_n = 1.78$. ^{1}H Nuclear Magnetic Resonance (NMR) (400 MHz, $CDCl_3$, d, ppm): 6.75 (2H, s), 6.35 (2H, s), 2.26–2.09 (4H, dd), 1.40–1.10 (broad, 12H). ATR-IR (cm^{-1}): 2995, 2864, 2239, 1605, 1446, 1264. Elemental analysis; $C_{29}H_{20}N_2O_4$ (*wt*%): C: 75.64, H: 4.37, N: 6.08 found: C: 72.2, H: 4.3, N:6.0. For electrospinning; PIM-1 (23% *w/v*) was dissolved in 1,1,2,2 tetrachloroethane and was stirred overnight for complete dissolution at room temperature. Then, it was electrospun as reported previously [42] under a voltage of 11–12 kV. The feeding rate of the solution was 0.5 mL h^{-1} and 18 cm tip to collector distance was fixed while using 2000 rpm rotation speed.

2.2.2. Synthesis and electrospinning of amide (hydrolyzed) PIM-1

The terms amide and hydrolyzed PIM-1 were used interchangeably throughout the manuscript. Synthesis of hydrolyzed PIM-1 powder was performed according to the previous method [42]. PIM-1 powder was hydrolyzed by NaOH (25% *w/v*) in H_2O/EtOH (1:1) mixture at 120 °C for 3h. Then, water was added to this solution and filtrated under vacuum. The powder was dried in an oven for overnight. Afterward, the sample was stirred in acidic water (pH: ~4) for 2 h and filtrated under vacuum. The sample was dried in an oven (110 °C) after washing with a copious amount of water. For electrospinning, hydrolyzed PIM-1 powder (70% *w/v*) was dissolved in DMF and was stirred for 4h at room temperature. Electrospinning was achieved using reported parameters [16], which were; 0.5 mL h^{-1} flow rate, 12 kV applied voltage, 15 cm distance.

2.2.3. Synthesis of electrospun amine PIM-1

Preparation of electrospun amine PIM-1 was conducted based on the previous method [18]. The fibrous membrane of PIM-1 (~0.3 g) was reacted with the borane-dimethylsulfide complex at 45 °C for overnight. Then, ethanol was used to quench the excess borane before placing the membrane in methanolic HCl (1 M). After that, the membrane was

neutralized by 5% (*w/v*) aqueous sodium hydroxide and washed with water followed by drying at 110 °C for overnight.

2.2.4. Synthesis and electrospinning of amidoxime PIM-1

Amidoxime modification was achieved according to the previously described procedure [17]. PIM-1 powder was dissolved in tetrahydrofuran (THF) and heated to 60 °C under an argon atmosphere. Then, hydroxylamine was added slowly (5 mL h^{-1}) by a syringe pump. The reaction was maintained at 69 °C for 23 h under reflux. The transparent solution was precipitated by ethanol and filtrated under vacuum. The white-off powder was obtained and it was dried at 110 °C in an oven for overnight. For electrospinning, amidoxime PIM-1 powder (40% *w/v*) was dissolved in DMF and it was stirred for 5h at room temperature. It was electrospun based on the parameters provided in our previous report [17] which were; 0.5 mL h^{-1} flow rate, 12 kV applied voltage, 16 cm distance.

2.3. Carbonization of PIM-1 and functionalized PIM-1 fibers

After evaporating the solvent residues at 110 °C; electrospun PIM-1 based fibrous mats were kept in the tubular furnace and purged with argon gas for 40 min to remove the oxygen from the tube. It is necessary to avoid oxidation or burning of PIM-1 based fibers during the pyrolysis process. The pyrolysis parameters were set as the maximum temperature at 800 °C with the ramp rate of 5 °C min^{-1} for 3 h, under continuous argon flow with the 100 sccm. After the pyrolysis, argon purging was continued until the furnace cools down to the room temperature then these CF were characterized and used for the ORR application. CF obtained from PIM-1, hydrolyzed PIM-1, amine PIM-1, and amidoxime PIM-1 are referred as CF-PIM-1, CF-hydrolyzed PIM-1, CF-amine PIM-1 and CF-amidoxime PIM-1, respectively.

2.4. Characterization

Thermogravimetric analysis (TGA) of PIM-1 based fibers was carried out to realize the decomposition process under N_2 atmosphere. TGA was carried out by heating the sample with the ramp rate of 20 °C until 600 °C. The morphology of electrospun PIM-1 based fibers and CF were monitored by FEI Quanta 200 FEG environmental scanning electron microscope (E-SEM) with an Everhart-Thornley Detector. Electrospun PIM-1 based fibers were sputtered by ~10 nm of gold before SEM measurements while CF were analyzed without gold coating by SEM. The average fiber diameters were calculated with the help of ImageJ software using at least 50 different fibers. Thermo K-alpha monochromatic high-performance X-ray photoelectron spectrometer (XPS) was used for the survey analyses (2 scans) and high resolution (50 scans) scans. High resolution elemental XPS was carried out with the pass energy, step size and spot size as 30 eV, 0.1 eV and 400 μm, respectively. The samples were examined by PANalytical X-ray Powder Diffractometer (XRD). The XRD measurements were using CuKα radiation (λ = 1.54 Å) in the range of $2\theta = 10^{o} - 90^{o}$. Quantachrome AutosorbiQ gas sorption analyzer was used to calculate Brunauer–Emmet–Teller (BET) surface areas which were determined from N_2 adsorption isotherms at 77K by multi-point analysis. For measuring BET, a small amount of PIM-1 based fibers and CF (~50 mg) were weighed into an analysis tube, degassed for 12 h under high vacuum at 120 °C and used for the further BET analysis. The confocal Raman Instrument (WITec alpha 300) was used to record Raman spectra. An average of at least 3 different points was characterized for each sample and plotted in the Raman figures. The attenuated total reflectance infrared (ATR-IR) spectra of fiber samples were measured by the Bruker Alpha P spectrometer for 32 scans at a resolution of 4 cm^{-1}.

2.5. Electrochemistry

All experiments were conducted using the Biologic SP-150 potentiostat with the standard three−electrodes electrochemical cell at room temperature. For the linear sweep voltammetry (LSV) measurements, free-standing CF-PIM-1, CF-hydrolyzed PIM-1, CF-amine PIM-1, and CF-amidoxime PIM-1 fibers were used as the working electrode without the support of glassy carbon electrode (GC). Whereas, to reveal the ORR kinetics and to understand the number of electrons involved in the ORR; electrocatalyst slurries were prepared by mixing 8 mg CF-PIM-1, CF-hydrolyzed PIM-1, CF-amine PIM-1, and CF-amidoxime PIM-1 fibers in the 500 μL of deionized water, 100 μL of ethanol, and 40 μL of 5 wt% Nafion solution followed by vortex for 10 min, individually. The standard Pt/C ink was prepared in the same way as mentioned above where 20% Pt/C was used instead of CF. The catalyst modified GC electrode (3 mm diameter, 0.07068 cm^2 of geometric surface area), Pt spiral wire and $Ag|AgCl|KCl_{(sat.)}$ were used as working, counter and reference electrodes, respectively for the rotating disc electrode (RDE) measurements. Prior to each experiment, the GC surface was cleaned with aqueous slurries of consecutively finer alumina powder (1.0 μm down to 0.06 μm) on the polishing micro-cloth. To remove the alumina adsorbed on the GC surface, the electrode was ultrasonically cleaned in the 18 MΩ Millipore water followed by ethanol for 10 min, individually. To fabricate CF-PIM-1, CF-hydrolyzed PIM-1, CF-amine PIM-1, CF-amidoxime PIM-1, and Pt/C modified GC, 4 μL electrocatalyst slurry was drop cast on the cleaned GC, individually. Thus, prepared electrodes were dried in an oven at 60 °C for 30 min prior to electrochemical measurements. All the ORR experiments were performed in 20 ml 0.1 M KOH solution. The electrolyte solutions were saturated with either N_2 or O_2 gas (99.999% of purity) for 45 min prior to the measurement. The RDE with LSV technique was used to determine ORR mechanism and kinetics. All the calculations were measured based on the geometric surface area unless specified. All the results measured vs. $Ag|AgCl|KCl_{(sat.)}$ were converted with respect to the reversible hydrogen electrode (RHE) using the Nernst equation (E1) [28,43]:

$$E_{RHE} = E_{Ag|AgCl|KCl(sat.)} + 0.059\ pH + E^{o}_{Ag|AgCl|KCl(sat.)} \quad (E1)$$

Where E_{RHE} is potential estimated vs. RHE, $E_{Ag|AgCl|KCl(sat.)}$ is measured potential vs. $Ag|AgCl|KCl_{(sat.)}$ electrode, $E^{o}_{Ag|AgCl|KCl(sat.)}$ is the standard electrochemical potential of the $Ag|AgCl|KCl_{(sat.)}$ electrode i.e. 0.197 V and pH of 0.1 M KOH is 13.

3. Results and discussion

Morphology of the electrospun PIM-1 based fibers was examined by scanning electron microscopy. The SEM images (Figs. 1 and S1) of (a1) PIM-1, (b1) hydrolyzed PIM-1, (c1) amine PIM-1, and (d1) amidoxime PIM-1 fibers show bead-free ultrathin fibers with the average diameters of 2.44 ± 0.17, 0.98 ± 0.27, 1.88 ± 0.08 and 1.31 ± 0.18 μm (Fig. 1 (a2-d2)) respectively. After pyrolysis, SEM images of the (a3) CF-PIM-1, (b3) CF-hydrolyzed PIM-1, (c3) CF-amine PIM-1, and (d3) CF-amidoxime PIM-1 show fibers remains intact. Moreover, the average fiber diameters did not show any significant change after pyrolysis (Fig. 1 (a4-d4)), showing the stability of PIM-1 based fibers in pyrolysis. Furthermore, it is interesting to notice that CF-amine PIM-1 and CF-amidoxime PIM-1 shows uniformly distributed holes on the fibers while CF-PIM-1 and CF-hydrolyzed PIM-1 does not show any holes. The weight of PIM-1, hydrolyzed PIM-1, amine PIM-1, and amidoxime PIM-1 fibers was reduced during the pyrolysis. After carbonization, the weight losses were measured and it showed 23%, 62%, 55% and 54% reduction for the CF-PIM-1, CF-hydrolyzed PIM-1, CF-amine PIM-1, and CF-amidoxime PIM-1 fibers. Since PIM-1 backbone contains aromatic structures, the decomposed parts are mostly dioxane splitting and they show variation based on the functional group, however, main fiber skeleton remains stable. The reduction in the fiber diameters are not as per the reduced weight yield, it might be due to the total decomposition of some PIM-1 based fibers or making the hollow CF which leads to pores in the CF-amine PIM-1 and CF-amidoxime PIM-1 fibers. In addition, the

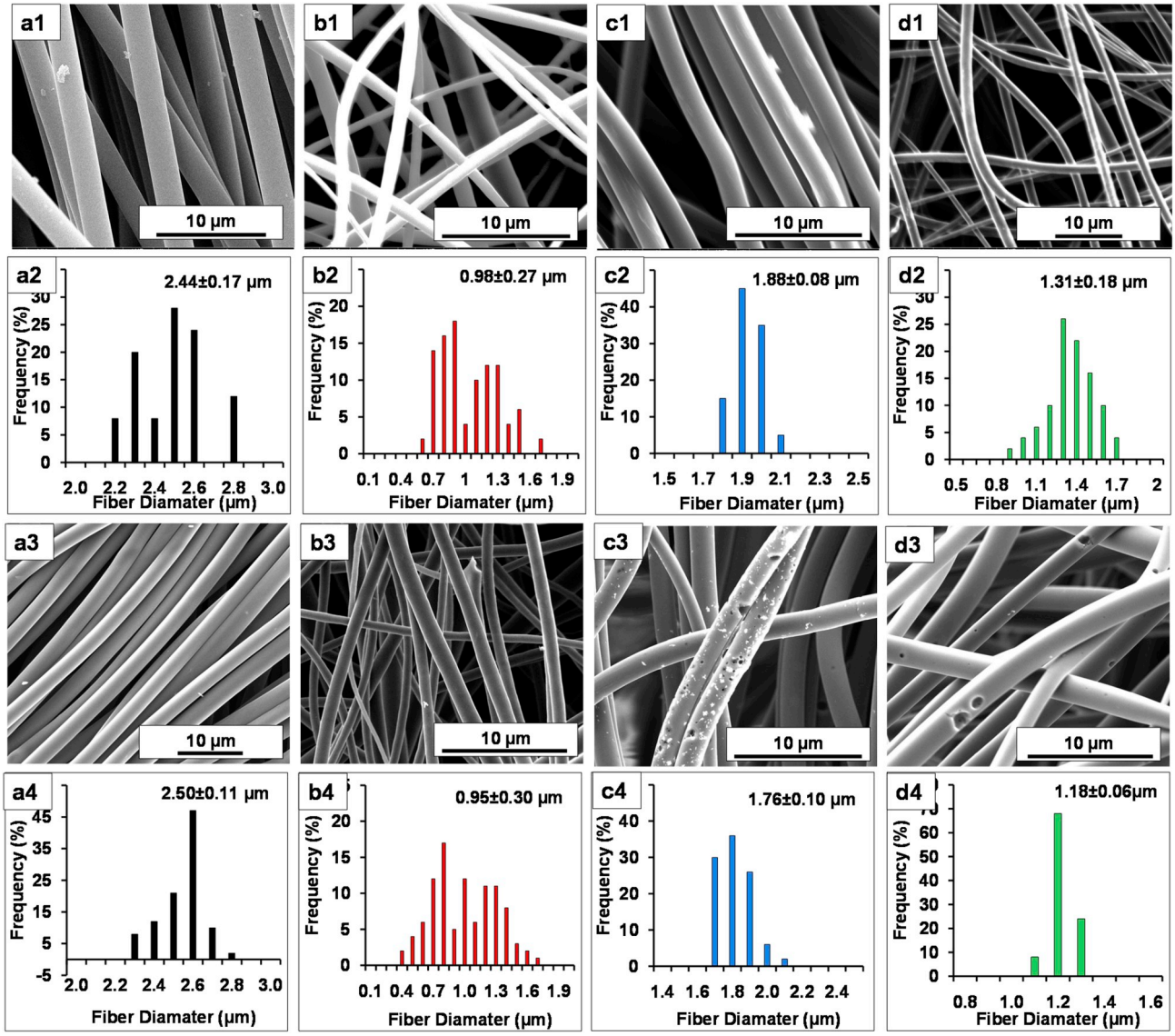

Fig. 1. Representative (1) SEM images and (2) average fiber diameter distributions of pristine PIM-1 based fibers (a) PIM-1, (b) hydrolyzed PIM-1, (c) amine PIM-1, and (d) amidoxime PIM-1. Representative (3) SEM images and (4) average fiber diameter distributions of the corresponding PIM-1 based CF samples.

possibility of a flow of some fiber mass during pyrolysis with the argon flow cannot be ruled out. Since the pyrolysis conditions are identical for all these fibers; the difference in the morphology is solely dependent on the functional group of PIM-1 based fibers.

Thermal decomposition of PIM-1 based fibers were performed using TGA as shown in Fig. 2 (a). TGA analysis of PIM-1 based fibers were conducted under N_2 atmosphere. PIM-1 fibers show decomposition after 450 °C [42] while amine PIM-1 and amidoxime PIM-1 fibers start decomposition at 320 °C and around 230–350 °C corresponding to the degradation of amine moiety and amidoxime groups, respectively [17,18]. However, in the case of hydrolyzed PIM-1 fibers, decomposition starts at 150 °C due to the decomposition of functional groups [16]. All these fibers show major decomposition after 450 °C which is polymer backbone degradation similar to the parent PIM-1 fibers. Thermal degradation of the PIM-1 follows dioxane splitting from 400 °C to 450 °C followed by complete dioxane and methyl group decomposition at ca. 450 °C [44,45]. Presence of oxygen during the thermal treatment decreases the temperature required for the thermal-oxidative degradation of these groups [44]. Thus, it is reasonable to observe decomposition of hydrolyzed PIM-1 (having oxygen attached with carbon by double bond which requires less energy for the decomposition than the hydroxyl group) at lowest temperature (i.e. 150 °C) than the amidoxime PIM-1 (having the hydroxyl group where decomposition initiates at 230–350 °C).

Functionalization of the PIM-1 based fibers with amide, amine, and amidoxime functional groups was confirmed by the FTIR spectra (Fig. 2 (b)) and their decomposition after pyrolysis were measured and plotted in Fig. 2 (c). The PIM-1 fibers show the characteristic nitrile stretches (2240 cm^{-1}) which reduced after functionalization with these functional groups. For hydrolyzed PIM-1 fibers, new bands emerged in the region 3000–3500 cm^{-1} along with a carbonyl peak at ~1700 cm^{-1} due to amide structure [17,39]. In the case of amine PIM-1 fibers, the peaks at the 3360 and 800 cm^{-1}, represents the N–H stretches [40], while amidoxime PIM-1 fibers have peaks at 3482, 3340 cm^{-1} of NH_2 stretching and 3175 cm^{-1} for O–H vibrations [41]. After carbonization, these peaks disappear which further proves successful pyrolysis of fibers. Formation of CF from PIM-1 based fibers was further confirmed with the XRD (Fig. 2d-g). It is well-documented that pristine PIM-1 or partially carbonized PIM-1 fibers show trimodal XRD pattern which disappears after pyrolysis and emergence of the broad peak at ca. 24° corresponds to graphene plane (100) [15,39]. In accordance with previous reports, we observed the same changes in the XRD pattern of CF-PIM-1.

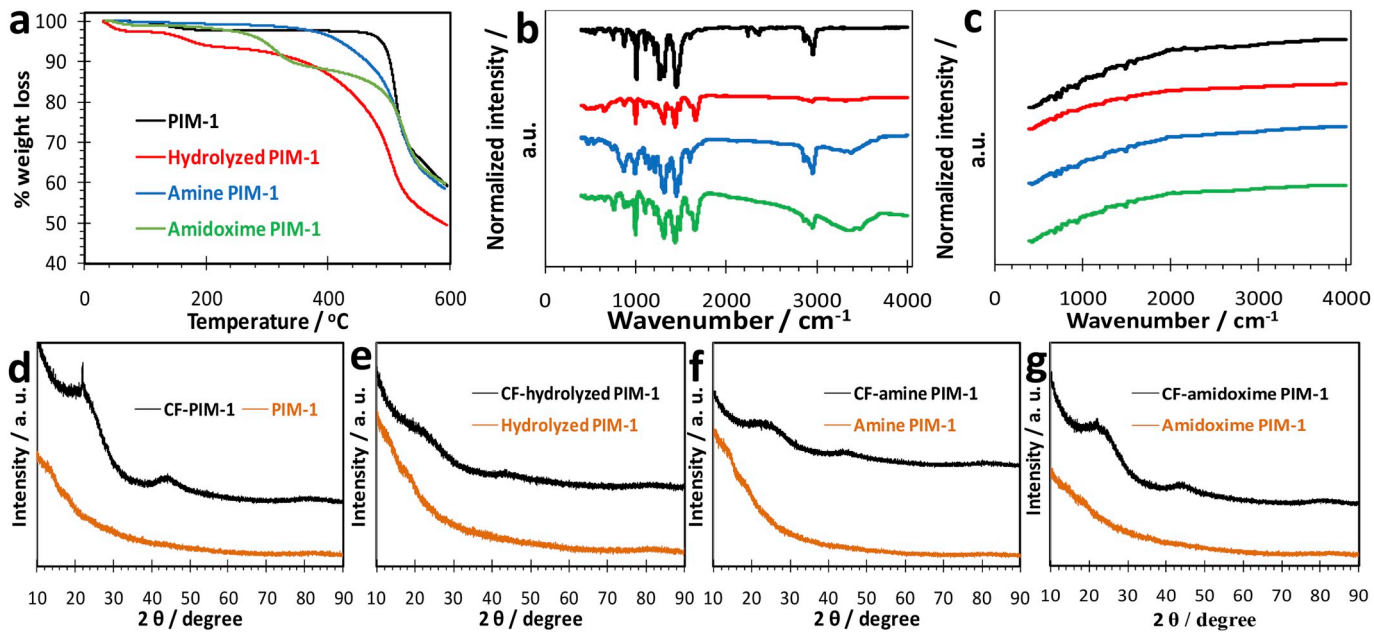

Fig. 2. (a) TGA curves and (b) FTIR spectra of PIM-1 (black), hydrolyzed PIM-1 (red), amine PIM-1 (blue), and amidoxime PIM-1 (green) fibers. (c) FTIR spectra of CF-PIM-1 (black), CF-hydrolyzed PIM-1 (red), CF-amine PIM-1 (blue), and CF-amidoxime PIM-1 (green) fibers. XRD analysis of (d) PIM-1, (e) hydrolyzed PIM-1, (f) amine PIM-1, (g) amidoxime PIM-1 fibers and their corresponding CF. (For interpretation of the references to colour in this figure legend, the reader is referred to the Web version of this article.)

Moreover, similar changes were also monitored for the CF from the PIM-1 based fibers, as represented in Fig. 2 (e to g). For verifying an influence of functional groups on the crystallization of the PIM-1 based CF, the average crystallite size of CF (Dc) were estimated from the Scherrer equation (E2) [46].

$$Dc = k \times \lambda / (\beta \times \mathrm{Cos}\ \theta) \quad \text{(E2)}$$

Where k is the Scherrer constant ($k = 0.9$) λ is the wavelength of x-ray, β is the full-width at half-maximum (FWHM), and θ is the Brag angle of XRD peak. The Dc values for the CF-PIM-1, CF-hydrolyzed PIM-1, CF-amine PIM-1, and CF-amidoxime PIM-1 fibers were 0.61, 0.76, 0.16, and 0.29, respectively (Fig. S2). The high value of Dc at the CF-hydrolyzed PIM-1 proves more graphitic phase among all these PIM-1 based CF [46].

The Raman spectra (Fig. 3) can be used to distinguish the sp^3 and sp^2 carbon in the CF by comparing the ID/IG ratios (Fig. S2) where the major peaks D and G band represents disordered and graphitic carbon [47]. The peaks at D3 and D4 represents sp^3-sp^2 carbon bonds and amorphous carbon, respectively [15]. Raman peak intensities of D and G bands were compared in the Table S1 and ID/IG ratios were calculated.

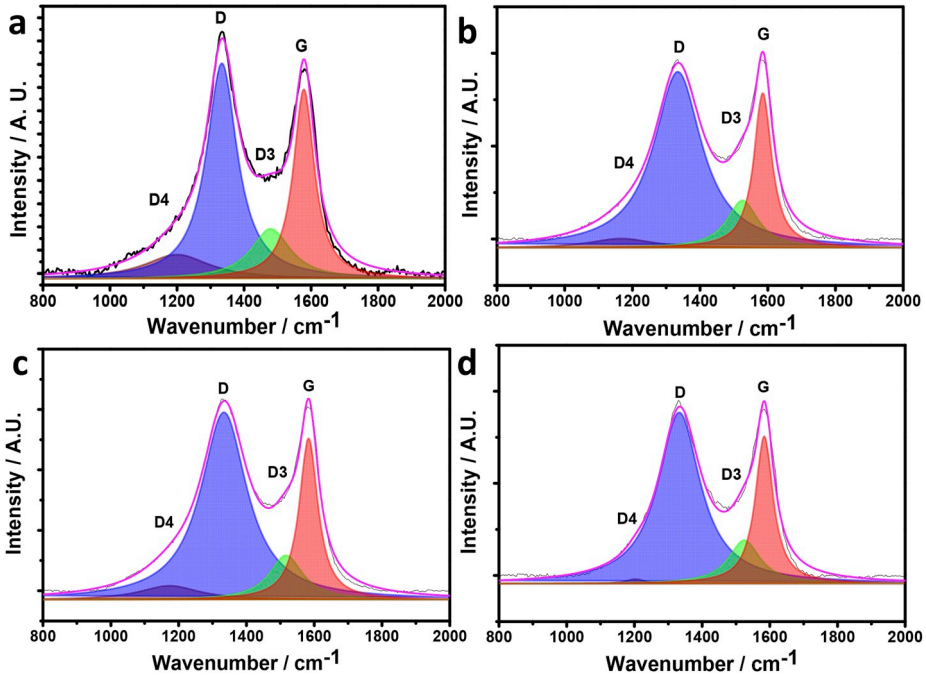

Fig. 3. Raman spectra of (a) CF-PIM-1, (b) CF-hydrolyzed PIM-1, (c) CF-amine PIM-1, and (d) CF-amidoxime PIM-1 fibers.

In the case of pristine PIM-1 based fibers, characterization by Raman is not possible with the selected wavelength (ʎ = 532 nm) of Raman due to the interference caused by the fluorescence properties of PIM-1 based fibers. Presence of D and G band which are the typical characteristic features of carbon further proves complete pyrolysis of PIM-1 based fibers into the CF. The ID/IG ratio of the CF-hydrolyzed PIM-1 is smallest i.e. 1.15 among all the CF obtained from PIM-1 based fibers. Although the carbonization process of PIM-1 based fibers is complex, since TGA and pyrolysis both are anaerobic carbonization they can be correlated. These Raman analyses are in agreement with the TGA results where hydrolyzed PIM-1 fibers decompose at low temperature than the other PIM-1 based fibers. The oxidative-degradation of hydrolyzed PIM-1 can oxidize the amorphous carbon which results in more graphitic carbon than the other PIM-1 based CF. The average crystallite size estimated by XRD also validates more graphitization in the CF-hydrolyzed PIM-1 (Fig. S2).

These results were further supported by porosity measurements. Figs. S3–S6 display N_2 adsorption/desorption isotherms, BET and pore size distribution graphs of pristine and carbonized PIM-1 based fibers. Additionally, calculated BET surface areas, total pore volumes and average pore diameters of the samples are provided in Table S2. As displayed in Figs. S3–S6, N_2 adsorption/desorption isotherms show hysteresis for pristine and carbonized PIM-1 based fibers. This is a common phenomenon for chars and microporous samples, particularly for PIM-1 samples [48]. The observed hysteresis is related to the availability and the shape of the pores which causes diffusion problems and thus, a difference in adsorption/desorption curves. Further, the BET surface area of PIM-1, hydrolyzed PIM-1, amine PIM-1, and amidoxime PIM-1 fibers were calculated which are 779, 74, 4, and 305 m^2/g respectively. These results are in agreement with the previous reports [16–18,42]. The amine PIM-1 fibers show the lowest surface area which might be either due to the possible partial cross-linking of the intermediate structure or strong hydrogen bonding of the amine moieties [19]. The hydrolyzed PIM-1 have lower surface area than PIM-1 and amidoxime PIM-1 fibers which might be either due to the strong hydrogen bonding or possible salt content in the structure from hydrolysis reaction. As we reported previously [16], hydrolyzed PIM-1 exhibits quite low surface area compare to powder form. This is possibly due to the strong interaction between hydrolyzed PIM-1 and spinning solvent (DMF). After pyrolysis the surface area of CF-PIM-1, CF-hydrolyzed PIM-1, CF-amine PIM-1 and CF-amidoxime PIM-1 changed into 52, 430, 180 and 230 m^2/g (Table S2). Thus, it is clear that the surface area of PIM-1 and amidoxime PIM-1 fibers decreased while hydrolyzed PIM-1 and amine PIM-1 fibers show an increase in the surface area after carbonization. The CF-hydrolyzed PIM-1 has a high surface area of 430 m^2/g while other CFs were below 250 m^2/g. In addition, pore size distributions of fibers before and after carbonization are provided in Figs. S3–S6 which reveals that average pore size reduces after carbonization for all samples. As shown in Table S2, CF-hydrolyzed PIM-1 also shows the highest pore volume and the smallest average pore size based on the N_2 adsorption/desorption measurements.

The effect of different functional groups of pristine PIM-1 based fibers on the chemical structure of CF was analyzed by the XPS analysis. The detailed XPS survey of PIM-1 based fibers before and after pyrolysis were plotted in Figs. S7 and S8. An increase in the carbon and decrease in the oxygen atomic percentage of CF (in comparison with pristine PIM-1 based fibers) shows their successful carbonization (Figs. S7 and S8). High resolution XPS of carbon were also compared before and after carbonization for the PIM-1 based fibers in Fig. 4(a–h). The peaks were deconvoluted into four major peaks corresponds to C–C/C═C, C–O–C/C–OH/C–N, O–C–O/C═O, and COOH/C═N at the binding energies of 284.8, 285.5, 286.0, and 288.0 ± 0.2 eV, respectively [49]. Pristine

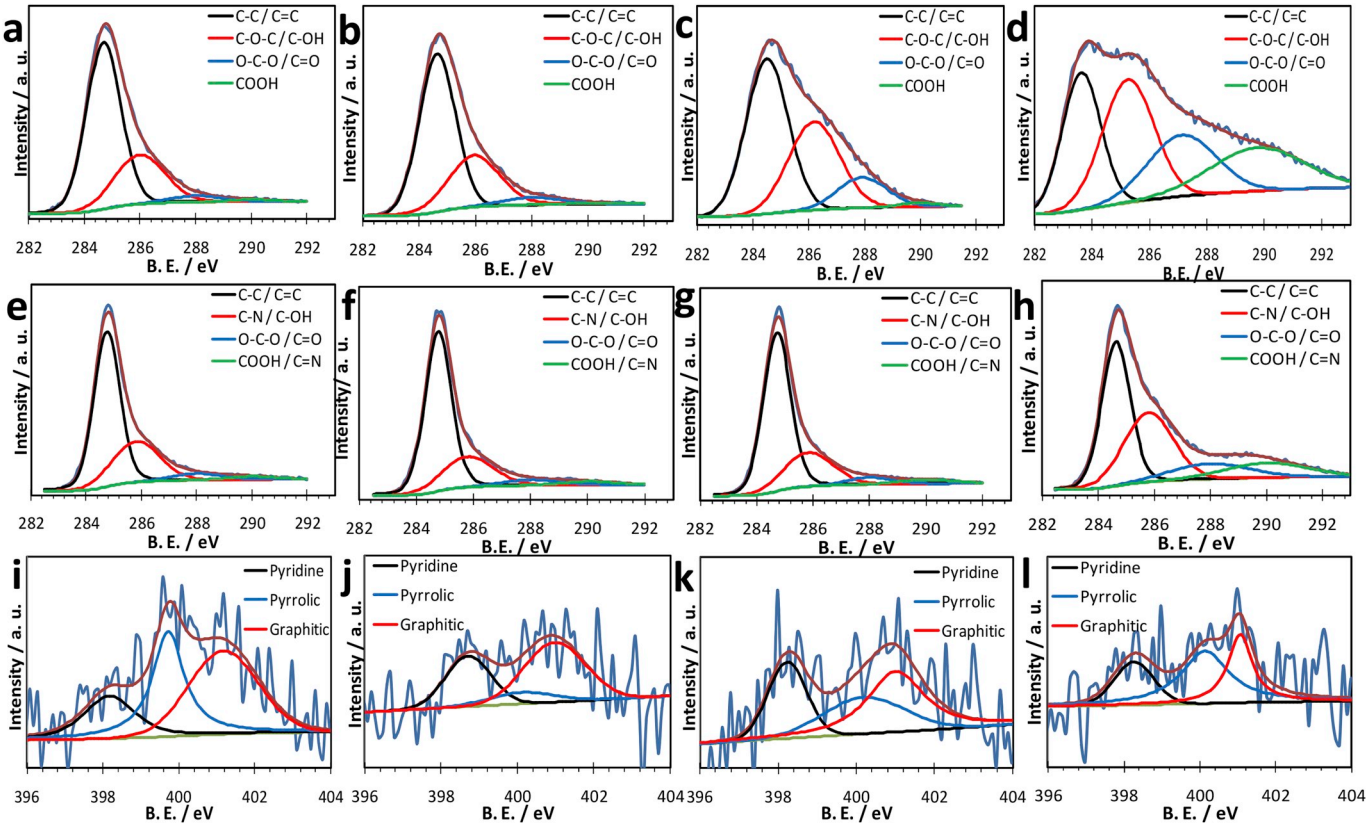

Fig. 4. High resolution carbon XPS of (a) PIM-1, (b) hydrolyzed PIM-1, (c) amine PIM-1, (d) amidoxime PIM-1, (e) CF-PIM-1, (f) CF-hydrolyzed PIM-1, (g) CF-amine PIM-1, and (h) CF-amidoxime PIM-1 fibers. High resolution nitrogen XPS of (i) CF-PIM-1, (j) CF-hydrolyzed PIM-1, (k) CF-amine PIM-1, and (l) CF-amidoxime PIM-1 fibers.

PIM-1 based fibers show decreased in the ratio of C–C/C═C (sp^2 carbon) to the oxidized carbon (i.e. C–OH/C–O–C, O–C–O/C═O, and COOH) from PIM-1 > hydrolyzed PIM-1 > amine PIM-1 > amidoxime PIM-1 fibers. These results are expected due to substitution of nitrile group of parent PIM-1 fibers with the C–O–NH_2, C–NH_2, NH_2–C═N–OH in the hydrolyzed PIM-1, amine PIM-1, and amidoxime PIM-1 fibers, respectively. After carbonization, the trend changes to CF-hydrolyzed PIM-1 > CF-amine PIM-1 > CF-PIM-1 > CF-amidoxime PIM-1 fibers. It further indicates more graphitic carbon in the hydrolyzed PIM-1 [46]. The atomic percentage of carbon increased and nitrogen is decreased after carbonization in all the CF (Figs. S7 and S8). It is clear that the decomposition of functional groups at low temperature (as shown in the TGA) leads to these changes in the atomic percentage after pyrolysis (Table S3).

Furthermore, we have analyzed high resolution nitrogen XPS (Fig. 4 (i - l)) to estimate the amount of nitrogen and the position of nitrogen in the carbon lattice. The nitrogen doping in the carbon can be of pyridinic, pyrrolic, and graphitic with binding energies of 398.3, 400.0, and 401.1 ± 0.2 eV, respectively [50,51]. Pyridinic and graphitic N-doped carbon were found more favourable for the ORR due to an auxiliary shift of an electron cloud by negative charges of doped nitrogen [20,52]. The atomic percentage from the XPS measurements of CF shows the amount of nitrogen doping was 2.96, 2.91, 1.68 and 1.66 in the CF-PIM-1, CF-amine PIM-1, CF-amidoxime PIM-1, and CF-hydrolyzed PIM-1, respectively. Although the amount of nitrogen is less in the CF-hydrolyzed PIM-1, the ratio of pyridinic + graphitic to pyrrolic nitrogen is highest as shown in Table S4.

For the ORR catalysis, onset potential and ORR kinetics (i.e. number of electrons involved in the ORR and Tafel slope) are two important parameters to select as the ORR catalyst. Since oxygen is reduced; anodic onset potential with four electron transfer ORR or in other words ORR with less applied potential without H_2O_2 production is the criteria for selecting ORR catalysts. These carbonized fibers were screened by the LSV and RDE measurements for the ORR kinetics. The LSV measured at the CF-PIM-1, CF-hydrolyzed PIM-1, CF-amine PIM-1, CF-amidoxime PIM-1, and Pt/C under O_2 saturated 0.1 M KOH solution is shown in Fig. 5a and S9 (a-e). These LSVs clearly showed the difference in the onset potential of ORR in the order of CF-PIM-1 > CF-amine PIM-1 > CF-amidoxime PIM-1 > CF-hydrolyzed PIM-1 > Pt/C. CF-hydrolyzed PIM-1 has ca. 50 mV and 30 mV anodic onset potential as compared with the CF-PIM-1 and CF-amine PIM-1 or CF-amidoxime PIM-1, respectively. The CF-PIM-1 has most cathodic (936 mV) while CF-hydrolyzed PIM-1 fibers (985 mV) shows most anodic ORR potential among these fibers which is close to the standard Pt/C onset catalyst (990 mV). Thus, CF-hydrolyzed PIM-1 is better ORR catalyst in terms of the onset potential.

To assess ORR kinetics, RDE measurements were carried out. An electrocatalytic activity of ORR obtained at the CF-PIM-1, CF-hydrolyzed PIM-1, CF-amine PIM-1, CF-amidoxime PIM-1 and Pt/C were analyzed with RDE measurements (rotation: 100–1600 rpm, scan rate: 10 mV s^{-1}) in the O_2 saturated 0.1 M KOH solution (Fig. 5b, S10) from positive to negative voltage. These RDE data were used for the Koutecky–Levich plots at the steady state currents (shown in Fig. S10). The Koutechy-Levich equitation (E3) was used to determine number of electrons (n) involved in the ORR per O_2 molecule [28,43,53].

$$1/j = 1/j_k + 1/j_L = 1/j_k + 1/(B\omega^{1/2}) \quad \text{(E3)}$$

Where B is $0.62nFCD^{2/3}\nu^{-1/6}$. The j_k, j, j_L, F, C, ν, D and ω are kinetic current density, measured or experimental current density, Levich current density, the Faraday constant, dissolved oxygen concentration, kinematic viscosity of the solution, diffusion coefficient of oxygen and rotation rate (rad s^{-1}), respectively [28,53]. The values for the F, C, ν, and D are 96,485 C mol^{-1}, 1.26×10^{-6} mol cm^{-3}, 1.009×10^{-2} $cm^2 s^{-1}$, 2.1×10^{-5} cm^2 s^{-1}, respectively. The number of electrons were estimated at four different potentials (Fig. 5c, S10) and the average number of electrons has the trend Pt/C ≥ CF-hydrolyzed PIM-1 > CF-amidoxime PIM-1 > CF-amine PIM-1 > CF-PIM-1. As per the ideal catalyst requirement, CF-hydrolyzed PIM-1 has a number of electrons ~4.0 similar to standard Pt/C catalyst which is considered as one of the best ORR catalysts so far.

For further evaluation of the ORR kinetics at these catalysts, the kinetic current density was calculated from equation (E4) [8] and used to estimate Tafel slope (Fig. 5d). Based on the slope and constant acquired from the straight line of log j_k vs. potential, Tafel slope and the exchange current density (i_0) were calculated.

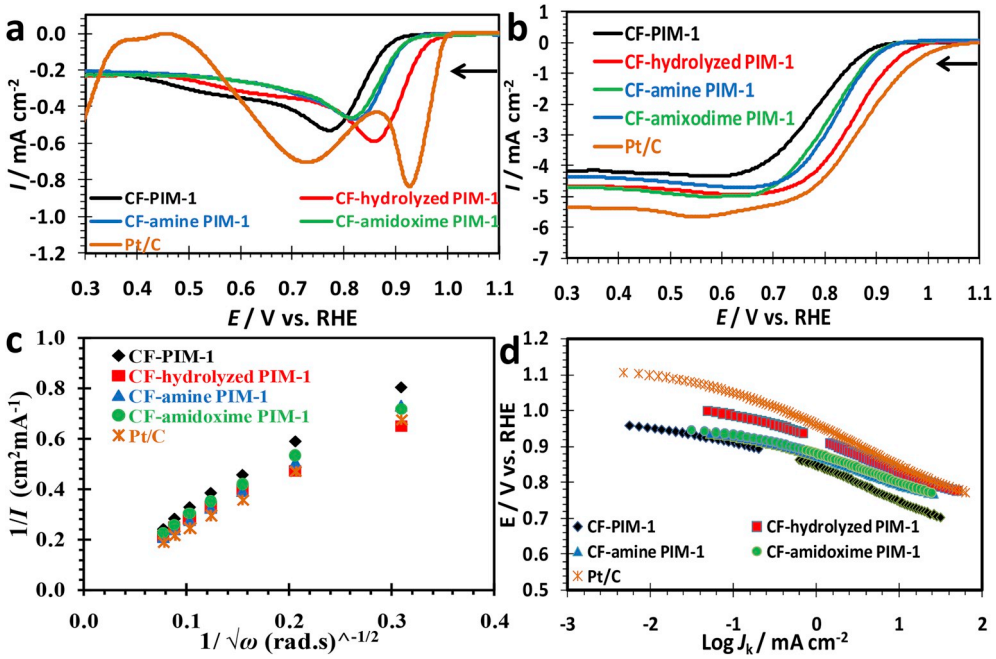

Fig. 5. (a) LSVs and (b) RDE (at 1600 rpm) under O_2 saturated 0.1 M KOH, at 10 mV s^{-1} vs. RHE. (c) The Koutecky–Levich plot (measured at the 0.4 V vs. RHE) and (d) Tafel slopes (data used from Fig. 5 b) obtained at CF-PIM-1 (black), CF-hydrolyzed PIM-1 (red), CF-amine PIM-1 (blue), CF-amidoxime PIM-1 (green), and Pt/C (orange). (For interpretation of the references to colour in this figure legend, the reader is referred to the Web version of this article.)

$$J_k = (j \times j_L)/(j_L - j) \quad \text{(E4)}$$

All these important catalytic properties were summarized in Table 1. The Tafel slopes were calculated at low current density (LCD) and high current density (HCD) corresponds to change in the adsorption intermediates from Temkin to Langmurian conditions [43]. In addition to these properties, half wave potential ($E_{1/2}$) and (i_0) are other parameters which equally influence the ORR [53]. The more anodic potential of $E_{1/2}$ and high value of i_0 are the qualities of an efficient ORR catalyst [43]. The high value of $E_{1/2}$ (847 mV vs. RHE) and i_0 (8.41 mA cm^{-2}) at CF-hydrolyzed PIM-1 makes it an efficient catalyst among these PIM-1 based CFs. ORR is one of the crucial steps in the fuel cell and metal air batteries both of which required a light material catalyst to design light weight energy devices. Thus, metal-free light-weight catalysts are necessary to replace high-cost noble Pt catalyst. CF-hydrolyzed PIM-1 ORR catalytic activity resembles the Pt. Furthermore, high half wave potential and exchange current density at CF-hydrolyzed PIM-1 made it better catalyst towards ORR than the CF-amine PIM-1, CF-amidoxime PIM-1, and CF-PIM-1. The onset potential at the CF-hydrolyzed PIM-1 and number of electrons involved in the ORR were close with the state-of-the-art Pt/C catalyst.

It is interesting to find out whether the catalysis is influenced solely by morphology or amount of nitrogen doped or position of nitrogen doping or as a cumulative effect of all. Based on the SEM images, it is evident that the small fiber diameters with non-porous structure of CF-hydrolyzed PIM-1 have better ORR catalysis than the porous fibers from CF-amine PIM-1 or CF-amidoxime PIM-1. Although the average pore size of CF-hydrolyzed PIM-1 (estimated from BET results) is the smallest, total pore volume of CF-hydrolyzed PIM-1 is greater than all carbonized samples. In contradictory, CF-PIM-1 are also non-porous fibers while its ORR catalytic activity is inferior to porous CF-amine PIM-1 and CF-amidoxime PIM-1. This result might be associated with CF-PIM-1's higher average fiber diameters and smaller pore volumes compared to CF-amine PIM-1 and CF-amidoxime PIM-1 fibers.

Thus, it is concluded that the morphology of CF is not the only factor which affects ORR catalysis [54]. Conductivity of CF can also influence the ORR and CF-hydrolyzed PIM-1 shows more graphitic carbon i.e. more conductivity than other CF based on PIM-1 fibers [46]. It is also supported by the Nyquist plot in Fig. S9f. The surface area has also an influence on ORR catalysis, and higher surface area is always preferable for the better catalysis which is confirmed by the performance of CF-hydrolyzed PIM-1. Furthermore, the amount of nitrogen doping can influence the ORR. The amount of nitrogen is in the order CF-PIM-1 > CF-amine PIM-1 > CF-amidoxime PIM-1 > CF-hydrolyzed PIM-1while ORR catalytic activity has reverse catalytic activity i.e. CF-hydrolyzed PIM-1 > CF-amidoxime PIM-1 > CF-amine PIM-1 > CF-PIM-1. The reports elaborated that amount of nitrogen linearly influence ORR catalysis [55] which is contradictory with present results (i.e. lower the amount of nitrogen doped in the carbon better the ORR catalytic activity for these selected carbon fibers). As per the Yang et al. conductivity is dominating over the amount of nitrogen in the CF [46]. Another possibility is the position of nitrogen in the carbon lattice which is found to be more crucial than the amount of nitrogen towards ORR catalysis. As reported previously, higher the pyridinic and graphitic nitrogen better the ORR catalysis which is applicable with the CF-hydrolyzed PIM-1. The durability of this catalysts and full cell performance needs to be further analyzed for the commercial viability of such N-doped catalysts. Overall, it is the combined effect of conductivity and nitrogen position in the CF which influences the ORR, which can be easily tuned by the modification of the functional group in the PIM-1 based fibers.

4. Conclusions

PIM-1 has been modified by functionalizing nitrile group to amide, amine, and amidoxime groups and bead-free ultrathin fibers were produced by electrospinning which were then pyrolyzed to obtain CF. The IR confirmed functionalization of PIM-1 fibers with the amide (peaks at 3000–3500 and ~1700 cm^{-1}), amine (peaks at 3360 and 800 cm^{-1}) and amidoxime (3482, 3340 and 3175 cm^{-1}) groups which disappear upon carbonization. The typical trimodal XRD peaks of PIM-1 fibers converted into broad peak around 24° further proves CF formation with all the PIM-1 based fibers. In addition, CF from PIM-1 and hydrolyzed PIM-1 have non-porous fibers while CF from amine PIM-1 and amidoxime PIM-1 have porous fibers. The amide and amidoxime groups change the thermal oxidative degradation of PIM-1 fibers due to presence of oxygen in the form of C═O and C–OH in their structure. Pyrolysis of hydrolyzed PIM-1 and amidoxime PIM-1 initiates their thermal degradation at low temperature (i.e. 150 and 230). The ID/IG ratios obtained from the Raman of CF have the trend of CF-amine PIM-1 > CF-PIM-1 or CF-amidoxime PIM-1 > CF-hydrolyzed PIM-1 indicating more graphitic carbon in the CF-hydrolyzed PIM-1 fibers. Thus, more conducting CF were obtained from the amide modified PIM-1 fibers. The amount of nitrogen in the CF from PIM-1, hydrolyzed PIM-1, amine PIM-1, and amidoxime PIM-1 were 2.96, 1.66, 2.91 and 1.68%, respectively. The overall influence of the morphological, amount of nitrogen and its position in the CF was revealed towards ORR catalysis under alkaline medium. The graphitic nature or conductivity and position of the nitrogen in the carbon lattice were found to be the most influencing conditions among these CF based on the PIM-1. Higher surface area (430 m^2/g), highest pore volume with smallest pore size, low amount of nitrogen (1.68%) and high percentage of pyridinic (34.29%) and graphitic (54.57%) nitrogen in the CF-hydrolyzed PIM-1 proved to be better ORR catalyst (onset potential 985 mV vs. RHE, ~ 4-electron transfer ORR with Tafel slope 87 (HCD)/54 (LCD) mV dec^{-1}) among these CF obtained from PIM-1 based fibers. These ORR catalytic activities are close to the standard Pt/C catalyst. Thus, properties of carbon fibers can be easily tuned by selecting the proper functional group of the PIM-1 based fibers. In addition to nitrogen group, oxygen and its binding energy with carbon can influence the CF formation by thermal-oxidative degradation of fibers by altering the conductivity of CF. In brief, amide functionalized or hydrolyzed PIM-1 fibers are easy to synthesize which after pyrolysis shows better ORR performance among the CF from PIM-1, amine PIM-1, and amidoxime PIM-1.

Table 1
Summary of ORR catalysis at the CF-PIM-1, CF-hydrolyzed PIM-1, CF-amine PIM-1, CF-amidoxime PIM-1 fibers, and Pt/C.

Sample	Onset potential	No. of electrons (n)	Tafel slope (HCD/LCD)	$E_{1/2}$ at1600 rpm	i_0/mA cm^{-2}
	mV vs. RHE		mV dec^{-1}	mV vs. RHE	
CF-PIM-1	936	3.48	98/42	777	7.17
CF-hydrolyzed PIM-1	985	3.98	87/54	847	8.41
CF-amine PIM-1	957	3.80	78/47	799	7.49
CF-amidoxime PIM-1	958	3.85	80/40	821	6.38
Pt/C	990	3.99	109/59	868	9.33

Declaration of competing interest

The authors declare that they have no known competing financial interests or personal relationships that could have appeared to influence the work reported in this paper.

Appendix A. Supplementary data

Supplementary data to this article can be found online at https://doi.org/10.1016/j.jpowsour.2020.227799.

References

[1] A. Hirsch, The era of carbon allotropes, Nat. Mater. 9 (2010) 868–871, https://doi.org/10.1038/nmat2885.

[2] M. Sharon, N. Mishra, B. Patil, A. Mewada, R. Gurung, M. Sharon, Conversion of polypropylene to two-dimensional graphene, one-dimensional carbon nano tubes and zero-dimensional C-dots, all exhibiting typical sp^2-hexagonal carbon rings, IET Circuits, Devices Syst. 9 (2015) 59–66, https://doi.org/10.1049/iet-cds.2014.0117.

[3] S. Osswald, G. Yushin, V. Mochalin, S.O. Kucheyev, Y. Gogotsi, Control of sp^2/sp^3 carbon ratio and surface chemistry of nanodiamond powders by selective oxidation in air, J. Am. Chem. Soc. 128 (2006) 11635–11642, https://doi.org/10.1021/ja063303n.

[4] J. Ni, Y. Li, Carbon nanomaterials in different dimensions for electrochemical energy storage, Adv. Energy Mater. 6 (2016) 1–21, https://doi.org/10.1002/aenm.201600278.

[5] A. Mewada, R. Vishwakarma, B. Patil, C. Phadke, G. Kalita, M. Sharon, M. Sharon, Non-blinking dendritic crystals from C-dot solution, Carbon Lett 16 (2015) 211–214, https://doi.org/10.5714/CL.2015.16.3.211.

[6] H. Dai, E.W. Wong, C.M. Lieber, Probing electrical transport in nanomaterials: conductivity of individual carbon nanotubes, Science 272 (1996) 523–526, https://doi.org/10.1126/science.272.5261.523.

[7] L. Duclaux, Review of the doping of carbon nanotubes (multiwalled and single-walled), Carbon 40 (2002) 1751–1764, https://doi.org/10.1016/S0008-6223(02)00043-X.

[8] A. Karatutlu, B. Patil, İ. Seker, S. Istengir, A. Bolat, O. Yildirim, et al., Structural, optical, electrical and electrocatalytic activity properties of luminescent organic carbon quantum dots, ChemistrySelect 3 (2018) 4730–4737, https://doi.org/10.1002/slct.201800714.

[9] T. Uyar, E. kny, Electrospun Materials for Tissue Engineering and Biomedical Applications: Research, Design and Commercialization, first ed., Elsevier, United Kingdom, 2017. Woodhead Publishing Series in Biomaterials.

[10] J. Xue, T. Wu, Y. Dai, Y. Xia, Electrospinning and electrospun nanofibers: methods, materials, and applications, Chem. Rev. 119 (2019) 5298–5415, https://doi.org/10.1021/acs.chemrev.8b00593.

[11] M.A. Khalily, B. Patil, E. Yilmaz, T. Uyar, Atomic layer deposition of Co_3O_4 nanocrystals on N-doped electrospun carbon nanofibers for oxygen reduction and oxygen evolution reactions, Nanoscale Adv 1 (2018) 1224–1231, https://doi.org/10.1039/c8na00330k.

[12] Y. Yang, A. Centrone, L. Chen, F. Simeon, T. Alan Hatton, G.C. Rutledge, Highly porous electrospun polyvinylidene fluoride (PVDF)-based carbon fiber, Carbon 49 (2011) 3395–3403, https://doi.org/10.1016/j.carbon.2011.04.015.

[13] R. Ruiz-Rosas, J. Bedia, M. Lallave, I.G. Loscertales, A. Barrero, J. Rodríguez-Mirasol, T. Cordero, The production of submicron diameter carbon fibers by the electrospinning of lignin, Carbon 48 (2010) 696–705, https://doi.org/10.1016/j.carbon.2009.10.014.

[14] J.S. Bonso, G.D. Kalaw, J.P. Ferraris, High surface area carbon nanofibers derived from electrospun PIM-1 for energy storage applications, J. Mater. Chem. A. 2 (2014) 418–424, https://doi.org/10.1039/c3ta13779a.

[15] B. Patil, B. Satilmis, M.A. Khalily, T. Uyar, Atomic layer deposition of NiOOH/Ni$(OH)_2$ on PIM-1-based N-doped carbon nanofibers for electrochemical water splitting in alkaline medium, ChemSusChem (2019) 1469–1477, https://doi.org/10.1002/cssc.201802500.

[16] B. Satilmis, P.M. Budd, T. Uyar, Systematic hydrolysis of PIM-1 and electrospinning of hydrolyzed PIM-1 ultrafine fibers for an efficient removal of dye from water, React. Funct. Polym. 121 (2017) 67–75, https://doi.org/10.1016/j.reactfunctpolym.2017.10.019.

[17] B. Satilmis, T. Isık, M.M. Demir, T. Uyar, Amidoxime functionalized Polymers of Intrinsic Microporosity (PIM-1) electrospun ultrafine fibers for rapid removal of uranyl ions from water, Appl. Surf. Sci. 467–468 (2019) 648–657, https://doi.org/10.1016/j.apsusc.2018.10.210.

[18] B. Satilmis, T. Uyar, Amine modified electrospun PIM-1 ultrafine fibers for an efficient removal of methyl orange from an aqueous system, Appl. Surf. Sci. 453 (2018) 220–229, https://doi.org/10.1016/j.apsusc.2018.05.069.

[19] B. Patil, Y. Kobayashi, S. Fujikawa, T. Okajima, L. Mao, T. Ohsaka, Direct electrochemistry and intramolecular electron transfer of ascorbate oxidase confined on l-cysteine self-assembled gold electrode, Bioelectrochemistry 95 (2014) 15–22, https://doi.org/10.1016/j.bioelechem.2013.10.005.

[20] Z. Chen, D. Higgins, H.S. Tao, R.S. Hsu, Z.W. Chen, Highly active nitrogen-doped carbon nanotubes for oxygen reduction reaction in fuel cell applications, J. Phys. Chem. C 113 (2009) 21008–21013, https://doi.org/10.1021/jp908067v.

[21] J. Suntivich, H.A. Gasteiger, N. Yabuuchi, H. Nakanishi, J.B. Goodenough, Y. Shao-Horn, Design principles for oxygen-reduction activity on perovskite oxide catalysts for fuel cells and metal-air batteries, Nat. Chem. 3 (2011) 546–550, https://doi.org/10.1038/nchem.1069.

[22] J.L. Fernández, V. Raghuveer, A. Manthiram, A.J. Bard, Pd-Ti and Pd-Co-Au electrocatalysts as a replacement for platinum for oxygen reduction in proton exchange membrane fuel cells, J. Am. Chem. Soc. 127 (2005) 13100–13101, https://doi.org/10.1021/ja0534710.

[23] M. Zhang, L. Dai, Carbon nanomaterials as metal-free catalysts in next generation fuel cells, Nano Energy 1 (2012) 514–517, https://doi.org/10.1016/j.nanoen.2012.02.008.

[24] H.A. Gasteiger, S.S. Kocha, B. Sompalli, F.T. Wagner, Activity benchmarks and requirements for Pt, Pt-alloy, and non-Pt oxygen reduction catalysts for PEMFCs, Appl. Catal. B Environ. 56 (2005) 9–35, https://doi.org/10.1016/j.apcatb.2004.06.021.

[25] J.P. McClure, R. Jiang, D. Chu, P.S. Fedkiw, Oxygen electroreduction on Fe-or Co-containing carbon fibers, Carbon 79 (2014) 457–469, https://doi.org/10.1016/j.carbon.2014.08.005.

[26] B. Lim, M. Jiang, P.H.C. Camargo, E.C. Cho, J. Tao, X. Lu, et al., Pd-Pt bimetallic nanodendrites with, Science 324 (2009) 1302–1305.

[27] F. Jaouen, E. Proietti, M. Lefèvre, R. Chenitz, J.P. Dodelet, G. Wu, et al., Recent advances in non-precious metal catalysis for oxygen-reduction reaction in polymer electrolyte fuel cells, Energy Environ. Sci. 4 (2011) 114–130, https://doi.org/10.1039/c0ee00011f.

[28] M.F. Tovini, B. Patil, C. Koz, T. Uyar, E. Yilmaz, Nanohybrid structured RuO_2/Mn_2O_3/CNF as a catalyst for Na-O_2 batteries, Nanotechnology 29 (2018) 475401 1–47540110, https://doi.org/10.1088/1361-6528/aadfb7.

[29] R. Cao, J.S. Lee, M. Liu, J. Cho, Recent progress in non-precious catalysts for metal-air batteries, Adv. Energy Mater. 2 (2012) 816–829, https://doi.org/10.1002/aenm.201200013.

[30] J. Huang, J. Han, T. Gao, X. Zhang, J. Li, Z. Li, P. Xu, B. Song, Metal-free nitrogen-doped carbon nanoribbons as highly efficient electrocatalysts for oxygen reduction reaction, Carbon 124 (2017) 34–41, https://doi.org/10.1016/j.carbon.2017.08.033.

[31] Z. Tang, Z. Pei, Z. Wang, H. Li, J. Zeng, Z. Ruan, et al., Highly anisotropic, multichannel wood carbon with optimized heteroatom doping for supercapacitor and oxygen reduction reaction, Carbon 130 (2018) 532–543, https://doi.org/10.1016/j.carbon.2018.01.055.

[32] J. Oh, S. Park, D. Jang, Y. Shin, D. Lim, S. Park, Metal-free N-doped carbon blacks as excellent electrocatalysts for oxygen reduction reactions, Carbon 145 (2019) 481–487, https://doi.org/10.1016/j.carbon.2019.01.056.

[33] S.M. Kim, Y.K. Heo, K.T. Bae, Y.T. Oh, M.H. Lee, S.Y. Lee, In situ formation of nitrogen-doped onion-like carbon as catalyst support for enhanced oxygen reduction activity and durability, Carbon 101 (2016) 420–430, https://doi.org/10.1016/j.carbon.2016.02.022.

[34] M.E.M. Buan, N. Muthuswamy, J.C. Walmsley, D. Chen, M. Rønning, Nitrogen-doped carbon nanofibers on expanded graphite as oxygen reduction electrocatalysts, Carbon 101 (2016) 191–202, https://doi.org/10.1016/j.carbon.2016.01.081.

[35] J. Tang, Y. Liu, G. Lv, C. Yang, G. Yang, Localized micro-deflagration induced defect-rich N-doped nanocarbon shells for highly efficient oxygen reduction reaction, Carbon 145 (2019) 411–418, https://doi.org/10.1016/j.carbon.2018.12.052.

[36] D. Yu, E. Nagelli, F. Du, L. Dai, Metal-free carbon nanomaterials become more active than metal catalysts and last longer, J. Phys. Chem. Lett. 1 (2010) 2165–2173, https://doi.org/10.1021/jz100533t.

[37] Y. Zheng, Y. Jiao, M. Jaroniec, Y. Jin, S.Z. Qiao, Nanostructured metal-free electrochemical catalysts for highly efficient oxygen reduction, Small 8 (2012) 3550–3566, https://doi.org/10.1002/smll.201200861.

[38] K. Gong, F. Du, Z. Xia, M. Durstock, L. Dai, Nitrogen-doped carbon nanotube arrays with high electrocatalytic activity for oxygen reduction, Science 323 (2009) 760–764, https://doi.org/10.1126/science.1168049.

[39] B. Satilmis, P.M. Budd, Base-catalysed hydrolysis of PIM-1: amide versus carboxylate formation, RSC Adv. 4 (2014) 52189–52198, https://doi.org/10.1039/c4ra09907a.

[40] C.R. Mason, L. Maynard-Atem, K.W.J. Heard, B. Satilmis, P.M. Budd, K. Friess, et al., Enhancement of CO_2affinity in a polymer of intrinsic microporosity by amine modification, Macromolecules 47 (2014) 1021–1029, https://doi.org/10.1021/ma401869p.

[41] H.A. Patel, C.T. Yavuz, Noninvasive functionalization of polymers of intrinsic microporosity for enhanced CO_2 capture, Chem. Commun. 48 (2012) 9989–9991, https://doi.org/10.1039/c2cc35392j.

[42] B. Satilmis, T. Uyar, Removal of aniline from air and water by polymers of intrinsic microporosity (PIM-1) electrospun ultrafine fibers, J. Colloid Interface Sci. 516 (2018) 317–324, https://doi.org/10.1016/j.jcis.2018.01.069.

[43] R. Mishra, B. Patil, F. Karadaş, E. Yılmaz, Bioinspired copper coordination polymer catalysts for oxygen reduction reaction, ChemistrySelect 2 (2017) 8296–8300, https://doi.org/10.1002/slct.201701303.

[44] Q. Song, S. Cao, R.H. Pritchard, B. Ghalei, S.A. Al-Muhtaseb, E.M. Terentjev, A. K. Cheetham, E. Sivaniah, Controlled thermal oxidative crosslinking of polymers of intrinsic microporosity towards tunable molecular sieve membranes, Nat. Commun. 5 (2014) 1–12, https://doi.org/10.1038/ncomms5813.

[45] O. Salinas, X. Ma, E. Litwiller, I. Pinnau, Ethylene/ethane permeation, diffusion and gas sorption properties of carbon molecular sieve membranes derived from the prototype ladder polymer of intrinsic microporosity (PIM-1), J. Membr. Sci. 504 (2016) 133–140, https://doi.org/10.1016/j.memsci.2015.12.052.

[46] D.S. Yang, S. Chaudhari, K.P. Rajesh, J.S. Yu, Preparation of nitrogen-doped porous carbon nanofibers and the effect of porosity, electrical conductivity, and nitrogen content on their oxygen reduction performance, ChemCatChem 6 (2014) 1236–1244, https://doi.org/10.1002/cctc.201400035.

[47] S. Bhardwaj, S.V. Jaybhaye, M. Sharon, D. Sathiyamoorthy, K. Dasgupta, P. Jagadale, et al., Carbon nanomaterial from tea leaves as an anode in lithium secondary batteries, Asian J. Exp. Sci. 22 (2008) 89–93.

[48] J. Jeromenok, J. Weber, Restricted access: on the nature of adsorption/desorption hysteresis in amorphous, microporous polymeric materials, Langmuir 29 (2013) 12982–12989, https://doi.org/10.1021/la402630s.

[49] S. Maldonado, S. Morin, K.J. Stevenson, Structure, composition, and chemical reactivity of carbon nanotubes by selective nitrogen doping, Carbon 44 (2006) 1429–1437, https://doi.org/10.1016/j.carbon.2005.11.027.

[50] H. Liu, Y. Zhang, R. Li, X. Sun, S. Désilets, H. Abou-Rachid, et al., Structural and morphological control of aligned nitrogen-doped carbon nanotubes, Carbon 48 (2010) 1498–1507, https://doi.org/10.1016/j.carbon.2009.12.045.
[51] Y. Shao, S. Zhang, M.H. Engelhard, G. Li, G. Shao, Y. Wang, et al., Nitrogen-doped graphene and its electrochemical applications, J. Mater. Chem. 20 (2010) 7491–7496, https://doi.org/10.1039/c0jm00782j.
[52] G. Liu, X. Li, P. Ganesan, B.N. Popov, Development of non-precious metal oxygen-reduction catalysts for PEM fuel cells based on N-doped ordered porous carbon, Appl. Catal. B Environ. 93 (2009) 156–165, https://doi.org/10.1016/j.apcatb.2009.09.025.
[53] T.G. Ulusoy Ghobadi, B. Patil, F. Karadas, A.K. Okyay, E. Yilmaz, Catalytic properties of vanadium diselenide: a comprehensive study on its electrocatalytic performance in alkaline, neutral, and acidic media, ACS Omega 2 (2017) 8319–8329, https://doi.org/10.1021/acsomega.7b01226.
[54] D.A. Links, S. Wohlgemuth, R.J. White, M. Willinger, M. Titirici, M. Antonietti, A one-pot hydrothermal synthesis of sulfur and nitrogen doped carbon aerogels with enhanced electrocatalytic activity in the oxygen reduction, Green Chem. (2012) 1515–1523, https://doi.org/10.1039/c2gc35309a.
[55] Z. Chen, Z. Chen, D. Higgins, Nitrogen doped carbon nanotubes and their impact on the oxygen reduction reaction in fuel cells, Carbon 48 (2010) 3057–3065, https://doi.org/10.1016/j.carbon.2010.04.038.